Application of desorption electrospray ionization mass spectrometry imaging in breast cancer margin analysis

David Calligaris[a,1], Diana Caragacianu[a,b,c,1], Xiaohui Liu[a,2], Isaiah Norton[a], Christopher J. Thompson[d], Andrea L. Richardson[e,f], Mehra Golshan[c], Michael L. Easterling[d], Sandro Santagata[e,f], Deborah A. Dillon[e], Ferenc A. Jolesz[b], and Nathalie Y. R. Agar[a,b,f,3]

Departments of [a]Neurosurgery, [b]Radiology, [c]Surgery, and [e]Pathology, Brigham and Women's Hospital, Harvard Medical School, Boston, MA 02115; [d]Bruker Daltonics, Billerica, MA 01821; and [f]Department of Cancer Biology, Dana–Farber Cancer Institute, Boston, MA 02215

Edited by Jerrold Meinwald, Cornell University, Ithaca, NY, and approved August 28, 2014 (received for review May 6, 2014)

Distinguishing tumor from normal glandular breast tissue is an important step in breast-conserving surgery. Because this distinction can be challenging in the operative setting, up to 40% of patients require an additional operation when traditional approaches are used. Here, we present a proof-of-concept study to determine the feasibility of using desorption electrospray ionization mass spectrometry imaging (DESI-MSI) for identifying and differentiating tumor from normal breast tissue. We show that tumor margins can be identified using the spatial distributions and varying intensities of different lipids. Several fatty acids, including oleic acid, were more abundant in the cancerous tissue than in normal tissues. The cancer margins delineated by the molecular images from DESI-MSI were consistent with those margins obtained from histological staining. Our findings prove the feasibility of classifying cancerous and normal breast tissues using ambient ionization MSI. The results suggest that an MS-based method could be developed for the rapid intraoperative detection of residual cancer tissue during breast-conserving surgery.

metabolites | FT-ICR MS | molecular pathology | intrasurgical diagnosis

Breast cancer is the most commonly diagnosed carcinoma in women in the United States and Western countries. Breast conservation surgery (BCS) has become the preferred treatment option for many women with early-stage breast cancer (1). BCS entails resection of the tumor, with a clean margin of normal tissue around it. Surgery is usually followed by radiation therapy. Results from seven large randomized prospective studies, with the largest two having over 20 y of follow-up, have shown equal survival when comparing BCS coupled with whole-breast radiation and mastectomy (2, 3).

Normally, breast surgeons aim to remove a patient's tumor, along with a rim of normal tissue that is free of cancer. Preoperative mammography, ultrasonography, or MRI may be used by the surgeon to guide adequate resection (4–6). Despite numerous improvements in imaging and surgical technique, the need for reexcision to achieve complete tumor resection in the United States typically ranges from 20–40% (7–15), and has been reported as being as high as 60% (16). The importance of reexcision is underscored by numerous studies, which have shown that incomplete resection of tumor and positive margins are associated with increased locoregional recurrence compared with negative margins (12, 17–20). Furthermore, the landmark meta-analysis performed by the Early Breast Cancer Trialists' Collaborative Group (18, 21) directly linked local recurrence to survival, placing great emphasis on the surgeon's role in minimizing local recurrence by obtaining adequate margins.

Breast tumor reexcisions are accompanied by a number of undesirable problems: The completion of therapy is delayed, infection rates are increased, cost is increased, there can be a negative psychological impact on the patient, and there can be diminished aesthetic outcomes (22–24). The development of an intraoperative technique that allows the fast and accurate identification of residual tumor at surgical resection margins could decrease the reexcision rate, and therefore improve the care delivered to patients with cancer who are receiving BCS.

To this end, multiple intraoperative methods have been explored, with various benefits as well as limitations. These methods include touch frozen section analysis (25), touch preparation cytology (26), specimen radiography (27, 28), rf spectroscopy (29, 30), Raman spectroscopy (31), radioguided occult lesion localization (32), near-IR fluorescence (33, 34), and high-frequency ultrasound (35–37). The intraoperative application of MRI, which has been successfully applied in brain surgery (38–42), is limited in its application in BCS. These limitations include MRI interpretation in the presence of acute surgical changes; lack of real-time imaging, requiring the interruption of surgery; and accurate localization of tumor based on images requiring development of fiducials (43–46).

Mass spectrometry imaging (MSI) has been applied to investigate the molecular distribution of proteins, lipids, and metabolites without the use of labels (47, 48). In particular, the newly developed ambient ionization technique of desorption electrospray ionization (DESI) allows direct tissue analysis with little to no sample preparation (49, 50). Therefore, with the advantage of easy use, DESI-MSI has great potential in the application of intraoperative tumor assessment. The development of DESI-MSI enables the correlation of lipid distribution in two or three dimensions with tissue morphology (47, 51) and the distinction of cancerous from noncancerous tissues based on lipidomic information (52–54). Distinctive

Significance

This study is the first demonstration, to our knowledge, of the application of desorption electrospray ionization mass spectrometry imaging (DESI-MSI) for discrimination of breast cancer and delineation of tumor margins. Using DESI-MSI, it is possible to discriminate between cancerous and adjacent normal tissue on the basis of the detection and specific spatial distributions of different lipid species. This study proves the feasibility of classifying cancerous and normal breast tissues using ambient ionization MSI. It will allow the surgeon to access to this information in real time so as to make accurate intraoperative decisions quickly. It will result in improved cosmesis and decrease the need for multiple operations for margin reexcision.

Author contributions: F.A.J. and N.Y.R.A. designed research; D. Calligaris, X.L., C.J.T., and M.L.E. performed research; A.L.R. and M.G. contributed new reagents/analytic tools; D. Calligaris, X.L., I.N., S.S., and D.A.D. analyzed data; A.L.R. and M.G. provided the samples; and D. Calligaris, D. Caragacianu, and N.Y.R.A. wrote the paper.

Conflict of interest statement: In compliance with Harvard Medical School and Partners Healthcare guidelines on potential conflict of interest, we disclose that S.S. and N.Y.R.A. are scientific advisors to BayesianDx.

This article is a PNAS Direct Submission.

[1]D. Calligaris and D. Caragacianu contributed equally to this work.

[2]Present address: School of Life Sciences, Tsinghua University, Beijing 100084, China.

[3]To whom correspondence should be addressed. Email: nathalie_agar@dfci.harvard.edu.

This article contains supporting information online at www.pnas.org/lookup/suppl/doi:10.1073/pnas.1408129111/-/DCSupplemental.

lipid profiles associated with different human cancers have been investigated by DESI-MSI (55–58). Moreover, the grades and subtypes of human brain tumors have been discriminated using this technique. Additionally, tumor margins have been delineated using DESI-MSI, and the results have been correlated with histopathological examination (59, 60).

It has been reported that breast cancer demonstrates metabolic profiles that are distinct from those metabolic profiles found in normal breast tissue. This finding suggests a potential for using metabolite information for breast cancer diagnosis and tumor margin identification (61, 62). Here, we demonstrate an MS-based methodology for using lipidomic information to distinguish cancerous from noncancerous tissue and to delineate tumor boundaries.

Results

Metabolite Profiling in Breast Cancer Tissues Using DESI-MSI. A DESI-MSI profile from the sample can be acquired quickly from a linear region of tissue on a slide (what is referred to as a line scan), or a more complete 2D molecular image can be acquired from a tissue section on a slide, yielding detailed spatial data that can be used to correlate underlying histology with the presence of signatures (multiple peaks) or specific single peaks (from one molecule). The line scan profile is appropriate for rapid data acquisition during a surgical procedure, whereas 2D molecular imaging is carefully done in the research setting to validate signatures relative to classic histopathology criteria. Here, we first demonstrate profiled mass spectra distinguishing normal and tumor tissues and then, in the section below, we present DESI-MSI data from 14 research subjects for more detailed validation.

The tissues from a total of 14 research subjects were analyzed using DESI-MSI. For each research subject, samples were taken at the tumor center, at the tumor edge, and 2 cm and 5 cm away from the tumor, as listed in Table 1. The samples from the contralateral breast were obtained from five research subjects who underwent double mastectomies. All of the samples were analyzed in negative ion mode in the *m/z* range of 50–1,100, meaning that the negative ions detected were predominantly lipid and metabolite species (47, 51, 54, 56, 59, 60). Compared with positive ion mode, the lipid spectra obtained from negative ion mode gave more unique information. Representative mass spectra from profiled breast cancer and nonneoplastic tissue sections are shown in Fig. 1 with corresponding optical images after histological staining. DESI-MS analysis, followed by standard H&E staining, was performed on the same tissue sections. This validation process has been made possible by using a nondestructive spray solvent (50:50 acetonitrile/dimethylformamide) to preserve tissue integrity during DESI-MSI analyses. Two healthy tissue samples were analyzed first. The first sample comprised breast lobules with epithelial cells (Fig. 1*A*), and the second comprised fibrous tissue mostly composed of fibroblasts and ECM (Fig. 1*B*). Most of the ions are detected in an *m/z* range between 700 and 1,000. According to previous studies, several peaks have been assigned to phospholipid (PL) species as phosphatidylinositol (PI), phosphatidylserine (PS), and phosphatidylethanolamine (59, 63–66) (*SI Appendix*, Table S1). We then confirmed the peak assignments by performing high-resolution MS using a Fourier transform ion cyclotron resonance (FT-ICR) mass spectrometer. The high-mass precision measurement of the FT-ICR analyzer allowed us to determine the elemental composition of the ions with a precision greater than 0.5 ppm during MS analyses (*SI Appendix*, Table S1) and to obtain structure information during tandem MS (MS/MS) analyses (*SI Appendix*, Table S2). From these two samples, series of lipid species present at nearly the same relative abundance [e.g., *m/z* 788.7 (i.e., PS18:0/18:1) and *m/z* 885.7 (i.e., PI18:0/20:4)] were identified (Fig. 1 *A* and *B*). Below *m/z* 500, most of the ions detected are background ions (Fig. 1 *A* and *B*). The overall signal acquired for fibrous tissue is less intense than for breast lobules due to a lower cell density, and therefore lower total lipid content (Fig. 1 *A* and *B*). In contrast, the profiled mass spectrum acquired from breast cancer tissue presents different relative intensities between the same PL peaks and ions of higher abundance in the *m/z* range of 500–700. Additional peaks in the low-*m/z* range (i.e., below *m/z* 500) are also detected (Fig. 1*C*). Using the DESI-MSI data from each of the 14 research subjects, we subtracted the average profile mass spectra of tumor tissue (Fig. 2*A*) from the average profile mass spectra of normal tissue (Fig. 2*B*) belonging to the same research subjects. Fig. 2*C* displays a "tumor-specific mass spectrum" that highlights all of the ions that could be taken into account to distinguish breast cancer tissue from normal breast tissue by DESI-MSI. Based on the profile mass spectra of Fig. 2*C*, all of the 14 research subjects have distinctive peak patterns in the low-mass region (Fig. 1*C*). We also performed high-mass resolution analyses to cross-validate the identification of these metabolites (discussion of sample preparation and MS analysis methods is provided in *SI Appendix*). We assigned with a precision greater than 0.5 ppm eight peaks present in the subtracted spectrum by an electrospray ionization FT-ICR MS analysis of a lipid extract from the center of a tumor sample from research subject 9 (*SI Appendix*, Table S1). MS/MS analyses allowed the identification of six of these peaks that are potentially

Table 1. Summarized description of samples from 14 research subjects

Subject no.	Tumor center	Tumor edge	2 cm away	5 cm away	Contralateral	Receptor status			Age, y	Sex
						ER	PR	Her2		
1	Y	Y	Y	Y	Y	Positive	Positive	Negative	42	Female
2	Y	Y	Y	Y	Y	Negative	Negative	Negative	63	Female
3	Y	Y	Y	Y	N	Positive	Positive	Negative	65	Male
4	Y	Y	Y	Y	N	Positive	Positive	Negative	76	Female
5	Y	Y	Y	Y	N	Positive	Positive	Negative	48	Female
6	Y	Y	Y	Y	N	Positive	Positive	Positive	46	Female
7	Y	Y	Y	Y	N	Positive	Positive	Negative	59	Female
8	Y	Y	Y	Y	N	Negative	Negative	Positive	60	Female
9	Y	Y	Y	Y	Y	Positive	Positive	Negative	38	Female
10	Y	Y	Y	Y	N	Positive	Positive	Negative	48	Female
11	Y	Y	Y	Y	N	Negative	Negative	Negative	64	Female
12	Y	Y	Y	Y	Y	Positive	Positive	Negative	47	Female
13	Y	Y	Y	Y	Y	Positive	Positive	Negative	38	Female
14	Y	Y	Y	Y	N	Positive	Positive	Negative	40	Female

N, no; Y, yes.

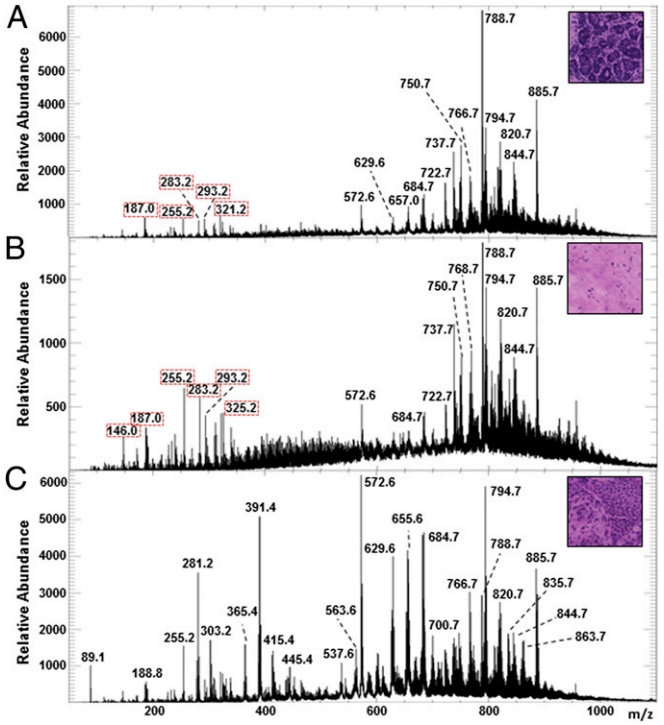

Fig. 1. Profiled mass spectra in negative ion mode using DESI-MSI located 5 cm away from tumor (*A*) and 2 cm away from tumor (*B*) tissue sections from research subjects 14 and 9, respectively, and a tumor center tissue section from research subject 14 (*C*). (*Right*) Histological images of representative tissue regions are shown. (Magnification, 40×.) The red-dashed outlines display background peaks.

markers of breast cancer (i.e., *m/z* 255.2, *m/z* 281.2, *m/z* 303.2, *m/z* 365.4, *m/z* 415.4, *m/z* 445.4 in *SI Appendix*, Table S1 and Figs. S1–S6). For *m/z* 391.4 and *m/z* 655.6, database searching using the LIPID Metabolites and Pathways Strategy database (www.lipidmaps.org/) listed a series of isobaric lipids for each *m/z* value (*SI Appendix*, Tables S3 and S4).

This distinctive subtracted tumor spectrum can be used for further targeted lipid identification and statistical analyses in the future to guide the intraoperative phenotyping of tumor tissue.

Toward a Breast Tumor Margin by DESI-MSI. DESI-MSI was performed on breast cancer samples from 14 research subjects to display 2D images correlating the lipid intensities with spatial distributions. Chemical information combined with the analysis of tissue morphology by standard light microscopy allows the differentiation of tumor and healthy tissue.

Fig. 3 includes the DESI MS images from samples of the tumor center, the tumor edge, and 2 cm and 5 cm away from the tumor, as well as from the contralateral breast of research subject 9. The ion maps of four representative ions [*m/z* 281.2 (oleic acid), *m/z* 391.4, *m/z* 655.6, and *m/z* 885.7 (PI18:0/20:4)] are displayed. All images are plotted with the same intensity scale. The lipid PI18:0/20:4, which is present in both healthy and tumor tissues, is used as a control to demonstrate successful ion detection. PI18:0/20:4 is abundant in tumor tissue (Fig. 3*A*) and in areas with normal mammary glands (Fig. 3 *C–E*). The histological images of the sections analyzed by DESI-MSI (sections from samples 2 cm and 5 cm away from tumor and from the contralateral side) confirm the specific localization of the PI18:0/20:4 in the breast lobules of the healthy tissue. However, distinct images were observed for ions with *m/z* 281.2, *m/z* 391.4, and *m/z* 655.6. These lipids are abundant at the tumor center, where there is high tumor cell density (Fig. 3*A*). These lipids are, however, absent or weak in normal tissue (Fig. 3 *C–E*). Interestingly, in the tissue section from the tumor edge (Fig. 3*B*), the tumor margin is sharply delineated by these ions (*m/z* 281.2, *m/z* 391.4, and *m/z* 655.6); high levels of the ions are observed in regions corresponding to tumor on the H&E-stained sections, whereas the ions are absent in the neighboring normal tissue. The ion with *m/z* 655.6 is still present, although very weak in normal cells (Fig. 3*B*).

Another example from research subject 14 is displayed in Fig. 4. Similarly, the ions at *m/z* 281.250 and *m/z* 391.4 are abundant in the tumor center (Fig. 4*A*) but are not detected in normal breast tissue 2 cm and 5 cm away from the tumor (Fig. 4 *C* and *D*). The ion with *m/z* 655.6 is present in regions corresponding to normal breast lobules and is less intense compared with tumor tissues. In a sample at the tumor edge, *m/z* 281.2 and *m/z* 391.4 are detected in an area containing stromal elements but no overt clusters of malignant cells (indicated by white arrows in Fig. 4*B*). This finding suggests that stromal elements adjacent to the tumor may contribute to the accumulation of these lipids.

Tumor and normal tissues were distinguished unambiguously based on a molecular image of characteristic metabolite profiles obtained from DESI-MSI. Further analyses of the data presented in Figs. 3 *A* and *D* and 4 *A* and *D* using SCiLS laboratory 2014a software (SCiLS GmbH) and global normalization provided results comparable to the original ion images (*SI Appendix*, Fig. S7).

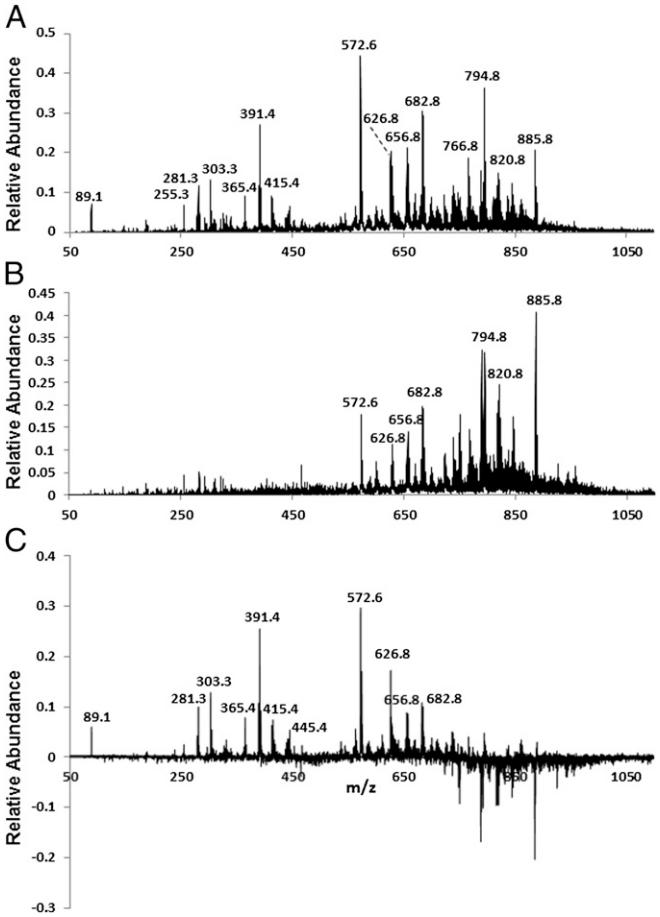

Fig. 2. Average of 14 normalized mass spectra from DESI-MSI analysis of tumor tissue (*A*) and average of 14 normalized mass spectra from DESI-MSI analysis of normal tissue (*B*). (*C*) Subtraction between the two first mass spectra (i.e., *A* − *B*).

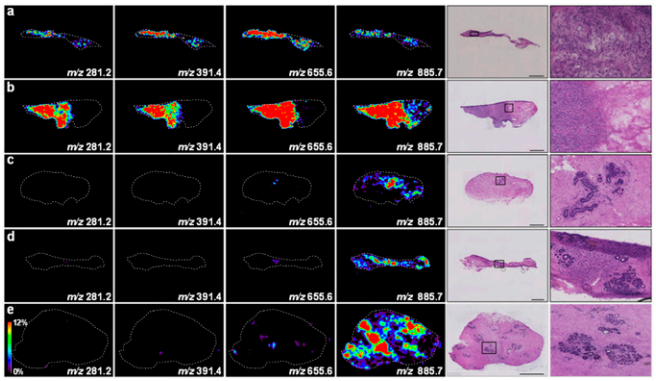

Fig. 3. DESI MS images from the tumor center (*A*), the tumor edge (*B*), 2 cm away from the tumor (*C*), 5 cm away from the tumor (*D*), and contralateral side (*E*) tissue sections from research subject 9 showing the distributions of ions at *m/z* 281.2, *m/z* 391.4, *m/z* 655.6, and *m/z* 885.7. (*Right*) Light microscopy images of the H&E-stained sections are shown. (Scale bars, 2 mm.)

Overall, 12 of 14 cases demonstrated striking differences between tumor and normal tissues in the distribution of the ions with *m/z* 281.2 and *m/z* 391.4. One of the two patients comprising the outlying cases is male, and a male breast has only a limited amount of breast tissue (mostly behind the nipple); thus, the interface of normal breast tissue and tumor rarely exists. The second patient is a perimenopausal woman without a reported history of pregnancy. Normal breast tissue presents such a wide range of physiological variations that it will require further investigation to challenge and validate the results reported here.

Potential Biomarker Characterization. Although the tumor tissue can be differentiated from healthy tissue simply by visualizing single peaks, such as *m/z* 281.2 (oleic acid), we conducted principal component analysis (PCA) and targeted lipid identification to increase the accuracy of the evaluation. PCA visualization of data from research subjects 9 and 14 showed separation of the spectra from tumor and normal tissues in both cases (Fig. 5). In Fig. 5*A*, the spectra from the tumor edge of research subject 9 clustered more closely to the tumor than did the distal normal samples, whereas those spectra from research subject 14 in Fig. 5*B* were not distinct from the distal normal samples. This observation is consistent with histopathological evaluation indicating that the tissue from the tumor edge of case 9 has a large tumor region (Fig. 3*B*), whereas the one from case 14 is mostly healthy tissue (Fig. 4*B*). In both cases, the tumor center spectra were distinctly clustered. Cross-validation between these two datasets was performed to evaluate the classification. Despite a limited sample number, clustering was also observed between the estrogen receptor (ER)-positive and progesterone receptor (PR)-positive tumor center specimens ($n = 10$) vs. ER-negative and PR-negative ($n = 3$) specimens (*SI Appendix*, Fig. S8). PCA of human epidermal growth factor receptor 2 (Her2)-positive ($n = 2$) and Her2-negative ($n = 11$) tumor center specimens, on the contrary, did not present an apparent separation.

Discussion

Failure to discern the margins of breast cancer adequately increases the likelihood of inadequate resection, resulting in higher risk of local recurrence. This fact underscores the importance of accurate margin assessment and complete tumor removal with lumpectomy. Our study is, to our knowledge, the first demonstration of MS use for the discrimination of breast cancer and the delineation of tumor margins. DESI-MSI is an effective technology for rapidly mapping lipid distributions on cell membranes, showing excellent histological specificity and tissue classification. This property facilitates diagnosis of cancer and detection of tumor extent (67, 68). In this feasibility study, the methodology of DESI-MSI was applied to discriminate human breast cancer from adjacent normal tissue using the gold standard H&E stain pathology evaluation as a comparison. The tissues from the tumor edge revealed distinctive molecular images consistent with tumor cell distributions, which were concordant with the interpretation by the breast pathologist, allowing the delineation of the tumor margin. In the profiled spectrum from negative ion mode, distinctive fatty acids and lipids were identified in breast cancer tissues. Studies indicated that medium- and long-chain free fatty acids are implicated in the activation of G protein-coupled receptors expressed in breast cancer cell lines (69–71). Some of these lipids are also known to be involved in the migration, proliferation, and invasion of breast cancer cells (i.e., oleic acid) or more generally in tumor processes (i.e., arachidonic acid) (69, 71–74). About 85% of samples have a significant increase in ion abundance in the low-mass region (i.e., below *m/z* 700) in tumor samples, whereas most ions in the high-mass range (e.g., *m/z* 885.7) exist in both the tumor and normal specimen. In the unique "tumor" spectrum, the positive ions (peaks with positive intensities) indicate the lipids abundant in the tumor; in contrast, the negative ions (peaks with negative intensities) imply the molecules from healthy cells. This unique peak pattern identification enables the diagnosis of cancerous tissue in seconds. This property has already been explored intraoperatively in neurosurgery, allowing for definition of margins and guidance of tumor resection (59, 75).

Although we were able to generate a metabolite print for breast cancer tissue that is distinctive from normal tissue in this feasibility study, we do recognize some limitations of DESI-MSI application. The data are generated from a very small number of samples. Furthermore, structural isomerism and stereoisomerism can complicate precise structural assignment (76). However, as we and others have shown, the absence of structural attribution in lipid analysis has not prevented lipid mapping by DESI-MSI. Other studies have shown that for diagnosis performed by DESI-MSI, identification of the lipids present in the mass spectra is not necessary for an empirical correlation of the histopathology and MS data (77). The fact that the characteristic tumor spectra are generated at the tumor center and tumor edge in contrast to unaffected regions from each research subject contributes to the specificity of the presented results. We have not yet tested this method for the detection and identification of skip lesions or

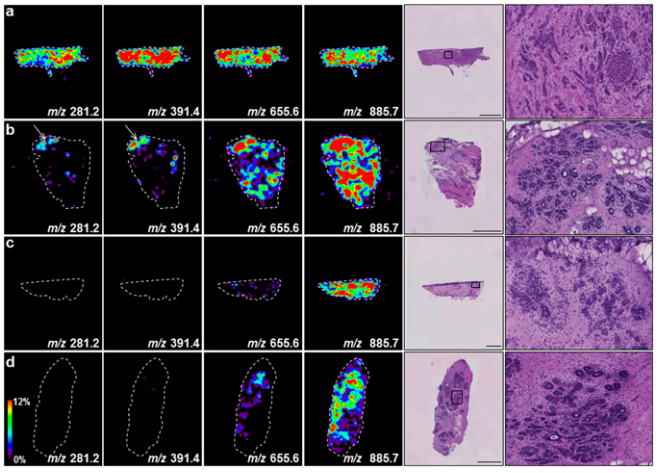

Fig. 4. DESI MS images from the tumor center (*A*), tumor edge (*B*), 2 cm away from the tumor (*C*), and 5 cm away from the tumor (*D*) tissue sections from research subject 14 showing the distributions of ions at *m/z* 281.2, *m/z* 391.4, *m/z* 655.6, and *m/z* 885.7. (*Right*) Light microscopy images of the H&E-stained sections are shown. (Scale bars, 2 mm.)

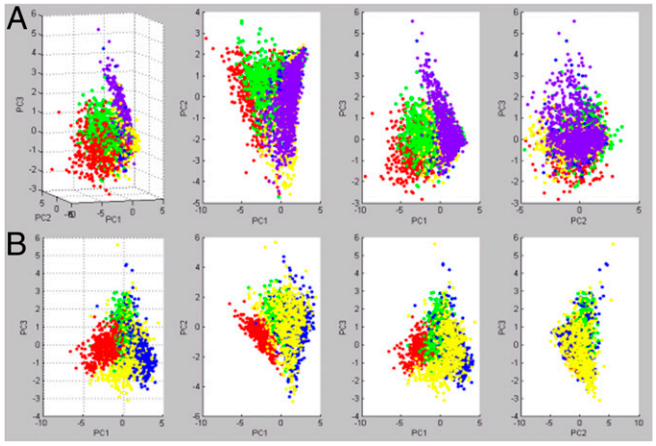

Fig. 5. PCA analysis of DESI-MSI data from mastectomy research subjects 9 (*A*) and 14 (*B*). For research subject 9, score plots of the three first principal components (PC1–PC3) display mass spectra from the tumor center group (red dots), tumor edge group (green dots), group located 2 cm away from the tumor (blue dots), group located 5 cm away from the tumor (yellow dots), and contralateral side group (purple dots). For research subject 14, score plots of the three first principal components (PC1–PC3) display mass spectra from the tumor center group (red dots), tumor edge group (green dots), group located 2 cm away from the tumor (blue dots), and group located 5 cm away from tumor (yellow dots).

multicentric lesions, but the results presented here will likely facilitate the development of an adequate clinical protocol to test our findings further. Our study was limited to invasive ductal carcinoma, but future studies will also be performed on ductal carcinoma in situ and invasive lobular carcinoma through the retrospective analysis of large numbers of banked specimens and dedicated intraoperative protocols.

Conclusion

This work illustrates the feasibility of the application of DESI-MSI as a promising lipidomic-based diagnostic tool in breast cancer. Classification of DESI-MSI data showed high recognition of breast cancer tissue. Additionally, DESI-MSI allowed discrimination between normal and cancerous tissue, hence delineating tumor margins. Further work mapping and characterizing these lipids will assist in increased specificity, identifying subtypes of breast cancer and hormone receptor status. The acquisition of this information will be more rapid than traditional standard means, allowing for more efficient adjuvant treatment planning. Thus far, these distinctive lipid profiles are easy and rapidly generated, allowing for the potential application of DESI-MSI in vivo intraoperatively in BCS to aid in margin assessment. The future direction of DESI-MSI research will be in conducting experiments in situ in lumpectomy cavities and/or on lumpectomy specimens.

Materials and Methods

Tissue Sample Preparation. All human tissue samples were obtained with informed consent and handled in accordance with approved Institutional Review Board protocols at the Brigham and Women's Hospital and Dana–Farber Cancer Institute. A total of 61 breast tissue samples encompassing tumor and adjacent tissue were obtained from 14 patients with breast cancer who underwent mastectomy at Brigham and Women's Hospital. The specimens were collected from the tumor center, tumor edge, and normal breast tissue 2 cm and 5 cm away from tumor, as well as from contralateral breast tissue when bilateral mastectomies were performed. Only cases with invasive ductal carcinoma histology were included in this study. The specimens were classified based on receptor status: ER, PR, and Her2 (78). Among the 14 cancers, nine were ER-positive, PR-positive, and HER2-negative (ER/PR^+, $HER2^-$); two were triple-negative (ER/PR^-, $HER2^-$); one was ER/PR^+, $HER2^+$; one was ER/PR^-, $HER2^+$; and one did not have receptor information available. The subjects comprised 13 female patients and 1 male patient, aged 38–76 y.

Samples were flash-frozen and stored in a freezer at −80 °C before analysis. The tissues were sectioned at a thickness of 12 μm using a Microm HM550 cryostat (Mikron Instruments, Inc.). A thickness of 20 μm was selected in several cases with fatty tissue. All samples were mounted on standard glass slides used for histology, which were dried in a desiccator before analysis.

DESI-MSI. All samples were analyzed using an AmazonSpeed mass spectrometer (Bruker Daltonics) connected to a commercial DESI source (Prosolia, Inc.). Additional details are provided in *SI Appendix*.

Histological Staining. Standard H&E staining was performed on the same tissue sections after DESI-MSI, as well as on serial sections to visualize tissue morphological information. All of the reagents used for H&E staining were purchased from Sigma–Aldrich. The optical tissue images were scanned using an Axio Imager M1 microscope (Zeiss) at a magnification of 40×. The morphology of tissue sections was evaluated on a Mirax Digital Slide Desktop Server system (Zeiss).

PCA Visualization. PCA clustering was conducted using ClinProTools version 2.3 (Bruker Daltonics) utilizing level scaling, peaking on total average spectrum, no peak limits, peak calculation by intensities, and an *m/z* range of 500–1,000.

ACKNOWLEDGMENTS. This work was funded, in part, by US National Institutes of Health Director's New Innovator Award 1DP2OD007383-01 (to N.Y.R.A.), US Army Medical Research/Center for Integration of Medicine & Innovative Technology Grant 2010A052245, and National Center for Image-Guided Therapy Grant P41RR019703. The work received support from the Pediatric Low-Grade Astrocytoma Program at Dana–Farber Cancer Institute, the Brain Science Foundation, and the Daniel E. Ponton Fund for the Neurosciences at Brigham and Women's Hospital.

1. Morrow M, et al. (2001) Factors predicting the use of breast-conserving therapy in stage I and II breast carcinoma. *J Clin Oncol* 19(8):2254–2262.
2. Fisher B, et al. (2002) Twenty-year follow-up of a randomized trial comparing total mastectomy, lumpectomy, and lumpectomy plus irradiation for the treatment of invasive breast cancer. *N Engl J Med* 347(16):1233–1241.
3. Veronesi U, et al. (2002) Twenty-year follow-up of a randomized study comparing breast-conserving surgery with radical mastectomy for early breast cancer. *N Engl J Med* 347(16):1227–1232.
4. Berg WA, et al. (2004) Diagnostic accuracy of mammography, clinical examination, US, and MR imaging in preoperative assessment of breast cancer. *Radiology* 233(3):830–849.
5. Wasif N, et al. (2009) MRI versus ultrasonography and mammography for preoperative assessment of breast cancer. *Am Surg* 75(10):970–975.
6. Jayender J, Chikarmane S, Jolesz FA, Gombos E (2014) Automatic segmentation of invasive breast carcinomas from dynamic contrast-enhanced MRI using time series analysis. *J Magn Reson Imaging* 40(2):467–475.
7. Leonetti JP, Brackmann DE, Prass RL (1989) Improved preservation of facial nerve function in the infratemporal approach to the skull base. *Otolaryngol Head Neck Surg* 101(1):74–78.
8. Mullenix PS, et al. (2004) Secondary operations are frequently required to complete the surgical phase of therapy in the era of breast conservation and sentinel lymph node biopsy. *Am J Surg* 187(5):643–646.
9. Lo CY, Kwok KF, Yuen PW (2000) A prospective evaluation of recurrent laryngeal nerve paralysis during thyroidectomy. *Arch Surg* 135(2):204–207.
10. Fleming FJ, et al. (2004) Intraoperative margin assessment and re-excision rate in breast conserving surgery. *Eur J Surg Oncol* 30(3):233–237.
11. Lorenz K, et al.; German Neuromonitoring Study Group (2010) What are normal quantitative parameters of intraoperative neuromonitoring (IONM) in thyroid surgery? *Langenbecks Arch Surg* 395(7):901–909.
12. Mandpe AH, Mikulec A, Jackler RK, Pitts LH, Yingling CD (1998) Comparison of response amplitude versus stimulation threshold in predicting early postoperative facial nerve function after acoustic neuroma resection. *Am J Otol* 19(1):112–117.
13. Camp ER, et al. (2005) Minimizing local recurrence after breast conserving therapy using intraoperative shaved margins to determine pathologic tumor clearance. *J Am Coll Surg* 201(6):855–861.
14. Kobbermann A, et al. (2011) Impact of routine cavity shave margins on breast cancer re-excision rates. *Ann Surg Oncol* 18(5):1349–1355.
15. Selesnick SH (1999) Optimal stimulus duration for intraoperative facial nerve monitoring. *Laryngoscope* 109(9):1376–1385.
16. McCahill LE, et al. (2012) Variability in reexcision following breast conservation surgery. *JAMA* 307(5):467–475.
17. Singer MC, Rosenfeld RM, Sundaram K (2012) Laryngeal nerve monitoring: Current utilization among head and neck surgeons. *Otolaryngol Head Neck Surg* 146(6):895–899.

18. Marcus B, et al. (2003) Recurrent laryngeal nerve monitoring in thyroid and parathyroid surgery: The University of Michigan experience. *Laryngoscope* 113(2):356–361.
19. Gage I, et al. (1996) Pathologic margin involvement and the risk of recurrence in patients treated with breast-conserving therapy. *Cancer* 78(9):1921–1928.
20. Mu L, Yang S (1991) An experimental study on the laryngeal electromyography and visual observations in varying types of surgical injuries to the unilateral recurrent laryngeal nerve in the neck. *Laryngoscope* 101(7 Pt 1):699–708.
21. Darby S, et al.; Early Breast Cancer Trialists' Collaborative Group (EBCTCG) (2011) Effect of radiotherapy after breast-conserving surgery on 10-year recurrence and 15-year breast cancer death: Meta-analysis of individual patient data for 10,801 women in 17 randomised trials. *Lancet* 378(9804):1707–1716.
22. Deutsch M, Flickinger JC (2003) Patient characteristics and treatment factors affecting cosmesis following lumpectomy and breast irradiation. *Am J Clin Oncol* 26(4): 350–353.
23. Cochrane RA, Valasiadou P, Wilson AR, Al-Ghazal SK, Macmillan RD (2003) Cosmesis and satisfaction after breast-conserving surgery correlates with the percentage of breast volume excised. *Br J Surg* 90(12):1505–1509.
24. Heil J, et al. (2012) Do reexcisions impair aesthetic outcome in breast conservation surgery? Exploratory analysis of a prospective cohort study. *Ann Surg Oncol* 19(2): 541–547.
25. McLaughlin SA, Ochoa-Frongia LM, Patil SM, Cody HS, 3rd, Sclafani LM (2008) Influence of frozen-section analysis of sentinel lymph node and lumpectomy margin status on reoperation rates in patients undergoing breast-conservation therapy. *J Am Coll Surg* 206(1):76–82.
26. Valdes EK, Boolbol SK, Cohen JM, Feldman SM (2007) Intra-operative touch preparation cytology; does it have a role in re-excision lumpectomy? *Ann Surg Oncol* 14(3): 1045–1050.
27. Abbas G, Heller KS, Khoynezhad A, Dubner S, Sznyter LA (2001) The incidence of carcinoma in cytologically benign thyroid cysts. *Surgery* 130(6):1035–1038.
28. Erguvan-Dogan B, et al. (2006) Specimen radiography in confirmation of MRI-guided needle localization and surgical excision of breast lesions. *AJR Am J Roentgenol* 187(2):339–344.
29. Joines WT, Zhang Y, Li C, Jirtle RL (1994) The measured electrical properties of normal and malignant human tissues from 50 to 900 MHz. *Med Phys* 21(4):547–550.
30. Karni T, et al. (2007) A device for real-time, intraoperative margin assessment in breast-conservation surgery. *Am J Surg* 194(4):467–473.
31. Haka AS, et al. (2006) In vivo margin assessment during partial mastectomy breast surgery using raman spectroscopy. *Cancer Res* 66(6):3317–3322.
32. Thomusch O, et al. (2004) Validity of intra-operative neuromonitoring signals in thyroid surgery. *Langenbecks Arch Surg* 389(6):499–503.
33. Thomusch O, Sekulla C, Walls G, Machens A, Dralle H (2002) Intraoperative neuromonitoring of surgery for benign goiter. *Am J Surg* 183(6):673–678.
34. Tomoda C, et al. (2006) Sensitivity and specificity of intraoperative recurrent laryngeal nerve stimulation test for predicting vocal cord palsy after thyroid surgery. *World J Surg* 30(7):1230–1233.
35. Gianfelice D, Khiat A, Amara M, Belblidia A, Boulanger Y (2003) MR imaging-guided focused ultrasound surgery of breast cancer: Correlation of dynamic contrast-enhanced MRI with histopathologic findings. *Breast Cancer Res Treat* 82(2):93–101.
36. Zippel DB, Papa MZ (2005) The use of MR imaging guided focused ultrasound in breast cancer patients; a preliminary phase one study and review. *Breast Cancer* 12(1): 32–38.
37. Furusawa H, et al. (2006) Magnetic resonance-guided focused ultrasound surgery of breast cancer: Reliability and effectiveness. *J Am Coll Surg* 203(1):54–63.
38. Risholm P, Golby AJ, Wells W, 3rd (2011) Multimodal image registration for preoperative planning and image-guided neurosurgical procedures. *Neurosurg Clin N Am* 22(2):197–206, viii.
39. Jolesz FA, et al. (2002) Intraoperative magnetic resonance imaging and magnetic resonance imaging-guided therapy for brain tumors. *Neuroimaging Clin N Am* 12(4): 665–683.
40. Black PM, et al. (1997) Development and implementation of intraoperative magnetic resonance imaging and its neurosurgical applications. *Neurosurgery* 41(4):831–842; discussion 842–835.
41. Schwartz RB, et al. (1999) Intraoperative MR imaging guidance for intracranial neurosurgery: Experience with the first 200 cases. *Radiology* 211(2):477–488.
42. Claus EB, et al. (2005) Survival rates in patients with low-grade glioma after intraoperative magnetic resonance image guidance. *Cancer* 103(6):1227–1233.
43. Yamashiro N, et al. (2009) Preoperative MRI marking technique for the planning of breast-conserving surgery. *Breast Cancer* 16(3):223–228.
44. Gould SW, Lamb G, Lomax D, Gedroyc W, Darzi A (1998) Interventional MR-guided excisional biopsy of breast lesions. *J Magn Reson Imaging* 8(1):26–30.
45. Sturgeon C, Sturgeon T, Angelos P (2009) Neuromonitoring in thyroid surgery: Attitudes, usage patterns, and predictors of use among endocrine surgeons. *World J Surg* 33(3):417–425.
46. Tomikawa M, et al. (2010) Real-time 3-dimensional virtual reality navigation system with open MRI for breast-conserving surgery. *J Am Coll Surg* 210(6):927–933.
47. Wiseman JM, Ifa DR, Song Q, Cooks RG (2006) Tissue imaging at atmospheric pressure using desorption electrospray ionization (DESI) mass spectrometry. *Angew Chem Int Ed Engl* 45(43):7188–7192.
48. Walch A, Rauser S, Deininger SO, Höfler H (2008) MALDI imaging mass spectrometry for direct tissue analysis: A new frontier for molecular histology. *Histochem Cell Biol* 130(3):421–434.
49. Takáts Z, Wiseman JM, Cooks RG (2005) Ambient mass spectrometry using desorption electrospray ionization (DESI): Instrumentation, mechanisms and applications in forensics, chemistry, and biology. *J Mass Spectrom* 40(10):1261–1275.
50. Donnellan KA, Pitman KT, Cannon CR, Replogle WH, Simmons JD (2009) Intraoperative laryngeal nerve monitoring during thyroidectomy. *Arch Otolaryngol Head Neck Surg* 135(12):1196–1198.
51. Eberlin LS, Ifa DR, Wu C, Cooks RG (2010) Three-dimensional vizualization of mouse brain by lipid analysis using ambient ionization mass spectrometry. *Angew Chem Int Ed Engl* 49(5):873–876.
52. Pirro V, Eberlin LS, Oliveri P, Cooks RG (2012) Interactive hyperspectral approach for exploring and interpreting DESI-MS images of cancerous and normal tissue sections. *Analyst (Lond)* 137(10):2374–2380.
53. Cooks RG, et al. (2011) New ionization methods and miniature mass spectrometers for biomedicine: DESI imaging for cancer diagnostics and paper spray ionization for therapeutic drug monitoring. *Faraday Discuss* 149:247–267; discussion 333–356.
54. Eberlin LS, et al. (2011) Desorption electrospray ionization then MALDI mass spectrometry imaging of lipid and protein distributions in single tissue sections. *Anal Chem* 83(22):8366–8371.
55. Masterson TA, et al. (2011) Distinctive glycerophospholipid profiles of human seminoma and adjacent normal tissues by desorption electrospray ionization imaging mass spectrometry. *J Am Soc Mass Spectrom* 22(8):1326–1333.
56. Calligaris D, et al. (2013) Mass spectrometry imaging as a tool for surgical decision-making. *J Mass Spectrom* 48(11):1178–1187.
57. Eberlin LS, et al. (2010) Cholesterol sulfate imaging in human prostate cancer tissue by desorption electrospray ionization mass spectrometry. *Anal Chem* 82(9):3430–3434.
58. Dill AL, et al. (2010) Multivariate statistical differentiation of renal cell carcinomas based on lipidomic analysis by ambient ionization imaging mass spectrometry. *Anal Bioanal Chem* 398(7-8):2969–2978.
59. Eberlin LS, et al. (2012) Classifying human brain tumors by lipid imaging with mass spectrometry. *Cancer Res* 72(3):645–654.
60. Eberlin LS, et al. (2010) Discrimination of human astrocytoma subtypes by lipid analysis using desorption electrospray ionization imaging mass spectrometry. *Angew Chem Int Ed Engl* 49(34):5953–5956.
61. Schlaepfer IR, et al. (2012) Progestin modulates the lipid profile and sensitivity of breast cancer cells to docetaxel. *Mol Cell Endocrinol* 363(1-2):111–121.
62. Hilvo M, et al. (2011) Novel theranostic opportunities offered by characterization of altered membrane lipid metabolism in breast cancer progression. *Cancer Res* 71(9): 3236–3245.
63. Dill AL, et al. (2011) Multivariate statistical identification of human bladder carcinomas using ambient ionization imaging mass spectrometry. *Chemistry* 17(10):2897–2902.
64. Girod M, Shi Y, Cheng JX, Cooks RG (2010) Desorption electrospray ionization imaging mass spectrometry of lipids in rat spinal cord. *J Am Soc Mass Spectrom* 21(7): 1177–1189.
65. He H, et al. (2007) Method for lipidomic analysis: p53 expression modulation of sulfatide, ganglioside, and phospholipid composition of U87 MG glioblastoma cells. *Anal Chem* 79(22):8423–8430.
66. Dill AL, et al. (2009) Lipid profiles of canine invasive transitional cell carcinoma of the urinary bladder and adjacent normal tissue by desorption electrospray ionization imaging mass spectrometry. *Anal Chem* 81(21):8758–8764.
67. Jackson SN, Wang HY, Woods AS (2005) Direct profiling of lipid distribution in brain tissue using MALDI-TOFMS. *Anal Chem* 77(14):4523–4527.
68. Gemoll T, Roblick UJ, Habermann JK (2011) MALDI mass spectrometry imaging in oncology (Review). *Mol Med Rep* 4(6):1045–1051.
69. Soto-Guzman A, Robledo T, Lopez-Perez M, Salazar EP (2008) Oleic acid induces ERK1/2 activation and AP-1 DNA binding activity through a mechanism involving Src kinase and EGFR transactivation in breast cancer cells. *Mol Cell Endocrinol* 294(1-2):81–91.
70. Navarro-Tito N, Robledo T, Salazar EP (2008) Arachidonic acid promotes FAK activation and migration in MDA-MB-231 breast cancer cells. *Exp Cell Res* 314(18):3340–3355.
71. Yonezawa T, Katoh K, Obara Y (2004) Existence of GPR40 functioning in a human breast cancer cell line, MCF-7. *Biochem Biophys Res Commun* 314(3):805–809.
72. Hardy S, St-Onge GG, Joly E, Langelier Y, Prentki M (2005) Oleate promotes the proliferation of breast cancer cells via the G protein-coupled receptor GPR40. *J Biol Chem* 280(14):13285–13291.
73. Navarro-Tito N, Soto-Guzman A, Castro-Sanchez L, Martinez-Orozco R, Salazar EP (2010) Oleic acid promotes migration on MDA-MB-231 breast cancer cells through an arachidonic acid-dependent pathway. *Int J Biochem Cell Biol* 42(2):306–317.
74. Soto-Guzman A, Navarro-Tito N, Castro-Sanchez L, Martinez-Orozco R, Salazar EP (2010) Oleic acid promotes MMP-9 secretion and invasion in breast cancer cells. *Clin Exp Metastasis* 27(7):505–515.
75. Eberlin LS, et al. (2013) Ambient mass spectrometry for the intraoperative molecular diagnosis of human brain tumors. *Proc Natl Acad Sci USA* 110(5):1611–1616.
76. Bennett IC, Greenslade J, Chiam H (2005) Intraoperative ultrasound-guided excision of nonpalpable breast lesions. *World J Surg* 29(3):369–374.
77. Hamelmann WH, Meyer T, Timm S, Timmermann W (2002) [A Critical Estimation of Intraoperative Neuromonitoring (IONM) in Thyroid Surgery]. *Zentralbl Chir* 127(5): 409–413. German.
78. Onitilo AA, Engel JM, Greenlee RT, Mukesh BN (2009) Breast cancer subtypes based on ER/PR and Her2 expression: Comparison of clinicopathologic features and survival. *Clin Med Res* 7(1-2):4–13.